# A Search for Active Galactic Nuclei Neutrinos using the MINOS Detector

A THESIS
SUBMITTED TO THE FACULTY OF THE GRADUATE SCHOOL
OF THE UNIVERSITY OF MINNESOTA
BY

Alden Michael Balmer

IN PARTIAL FULFILLMENT OF THE REQUIREMENTS
FOR THE DEGREE OF
MASTER OF SCIENCE

Professor Marvin L. Marshak, Advisor
School of Physics & Astronomy

January 2011

## Table of Contents

## List of Tables

## List of Figures

## I. Background

High energy neutrinos, greater than 1 GeV and up to several TeV, are generally thought to originate from Active Galactic Nuclei (AGN). Lower energy neutrinos in the neighborhood of 1 GeV or less are known to originate from the sun and from other stars. The cosmic accelerator model is used to explain the production of neutrinos from AGN. This theory hypothesizes that protons are accelerated by electromagnetic energy in extended magnetic fields close to a massive black hole. Particles are accelerated to relativistic speeds in the accretion disk surrounding the black hole through diffusive acceleration mechanisms [4]. These cosmic accelerators are thought to produce pions that can produce huge quantities of high energy neutrinos capable of escaping the AGN [7]. Neutrinos carry no charge, have extremely small mass ($<190$ keV/$c^2$), and interact infrequently with other matter, therefore, indirect methods are used for detecting them. Cosmic neutrinos interact with matter to produce electrons and muons. These particles decay to produce muons which can be tracked using scintillators to detect light bursts resulting from ionization and recombination along the path traveled. Neutrinos come in three flavors, muon ($\nu_\mu$), electron ($\nu_e$) and tau ($\nu_\tau$). Each neutrino flavor produces its corresponding flavor particle by charged current interaction. That is, the muon neutrino can produce a detectable muon. The high energy muon neutrino momentum transfers to the charged muon particle. The muon carries charge and therefore can be tracked. Cosmic rays, consisting of very high energy hadrons, produce downward traveling muons from reactions occurring in the atmosphere. The MINOS detector located in Soudan, Minnesota was constructed to study neutrinos produced at the Fermilab accelerator in Batavia, Illinois. The neutrinos are beamed 735 km through the earth to the detector. The detector is 700 m below ground in a mine converted into an underground laboratory. It consists of layers of plastic scintillator sheets sandwiched between steel absorber sheets instrumented with approximately 1500 photomultiplier tubes (PMT). Muons created by particle interactions between the neutrino beam and matter in the surrounding rock or within the detector itself produce detectible muon tracks. The goal for this paper, however, was to use the MINOS detector to look at cosmic neutrinos instead of the

neutrinos beamed from Fermilab. This was done to test the hypothesis that AGN are sources of detectable high energy neutrinos. Attempting to detect muons produced by AGN neutrinos is complicated somewhat because cosmic rays also produce high energy muons that are mixed in with the cosmic neutrino muons. Fortunately, there is a convenient way around this. Cosmic ray muons are effectively limited to about a 4 km travel distance through the earth whereas neutrinos travel nearly unimpeded through the entire earth. Therefore, the earth can act as a filter to allow up-going neutrinos to pass through from below to interact and produce detectable muons within rock formations in the vicinity of the detector.

## II. Neutrino Detectors

Since only a very small fraction of neutrinos interact with matter, neutrino detectors tend to be very large and massive to increase the likelihood that an interaction occurs and that a detectible byproduct such as a muon or an electron is produced and detected. For the study of AGN source neutrinos, the detector must have the capability of detecting atmospheric neutrinos. This kind of detector is typically located underground to shield it from particles created by cosmic rays. There are several neutrino detection sites that are in operation or were previously in operation worldwide. Each of these sites has particular capabilities inherent to the detector design and detection methodology used. Some of these detectors have been used in attempts to search for AGN sources of neutrinos. A brief description of the methodologies and capabilities of each of these sites follows.

### a. Main Injector Neutrino Oscillation Search (MINOS)

The MINOS far detector, located in Soudan, Minnesota and shown in Figure 1, is the detector used in this study. It is a sampling calorimeter detector made out of alternating planes of 2.54 cm thick toroidally magnetized steel sheets and 1 cm thick by 4.1 cm wide extruded polystyrene plastic scintillator strips. The plastic strips are arranged side-by-side diagonal to the vertical to cover one layer and then again in the opposite diagonal direction for the adjacent layer as shown in Figure 2. This arrangement allows capturing

a stereoscopic image of a muon track through the detector. The detector is oriented in a northwest-southeast direction such that the Z-axis points northwest and the Y-axis points up. The neutrino beam produced at Fermilab first passes through a near detector located 1 km from the source. This is done to characterize the beam. The neutrino beam then travels through the earth for 735 km and finally enters the far detector in Soudan from the southeast [9]. Magnetization averaging 1.42 T is achieved in each of two sections by passing a current carrying cable through the center of the steel plates and around the outside to form a loop. This arrangement provides a means of measuring muon momentum based on track curvature with a resolution of $\sigma_P/P \sim 12\%$ for muons with energies greater than 2 GeV. The magnetized steel sheets are also used to determine the charge polarity of the muons and thereby determine whether an incident neutrino or anti-neutrino produced the muon.

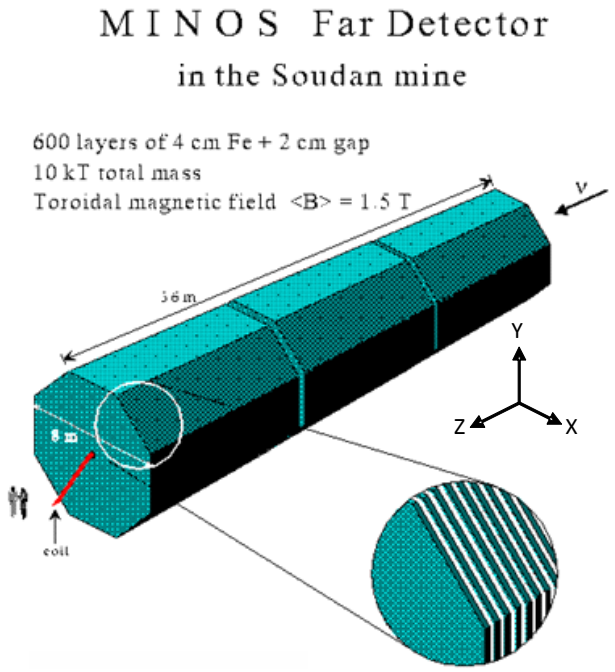


Figure 1. An early concept illustration of the MINOS detector at Soudan mine in Minnesota. The detector that was constructed consists of two sections instead of the three shown here [28].

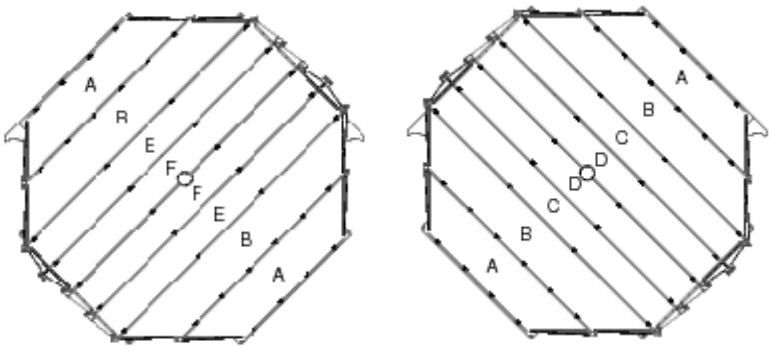


Figure 2. These are illustrations of two adjacent layers of 486 total layers in the MINOS far detector that show how the scintillator strips are arranged. These adjacent layers are referred to as transverse U (left) and V (right) planes. Each layer is approximately 8 m wide by 8 m high. The areas labeled A, B, C, etc. contain the plastic scintillator strips laying side-by-side. As a muon travels through the detector, the individual scintillator strips detect light pulses. The crosswise arrangement of the strips isolates the path in 3D that the muon follows [9].

### b. Super Kamiokande

The Super Kamiokande detector shown in Figure 3 and located 1,000 m underground in the Kamioka Mining and Smelting Company Mozumi Mine near Hida, Gifu Prefecture, Japan, consists of a large volume, 50,000 tons, of ultra-pure water surrounded by photomultiplier tubes (PMT). It is used to detect Cherenkov radiation when incident neutrinos interact with the water and produce either muons or electrons. Cherenkov radiation is produced by either the muon or electron velocity exceeding the velocity of light in the water. This produces a cone shaped shock wave at about a 40-degree angle from the particles trajectory. The water is contained in a 50,220 cubic meter tank populated with 11,146 PMTs. It was originally constructed in 1983 for the purpose of testing the theory of proton decay and then, later, to study solar neutrino interactions. In 1996 it was expanded and upgraded to conduct fundamental research on neutrinos. The

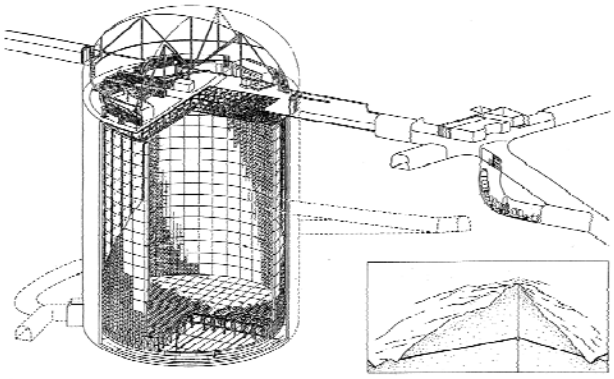

Figure 3 Super Kamiokande detector [14].

expanded detector is in the same mine but located at a slightly different place. It has an angular resolution of 26 degrees and an energy range of $10^6$ to $10^{21}$ eV.

### c. Sudbury Neutrino Observatory (SNO)

The Sudbury Neutrino Observatory illustrated in Figure 4 is located about 2,000 m underground at the Vale Inco's Creighton Mine in Sudbury, Ontario, Canada, an active nickel mine. SNO operated from 1999 through 2006. It was constructed primarily to study solar neutrinos. The detector is a sphere containing 1,102 tons of heavy water to shield out radioactivity from nearby sources. It is instrumented with about 9,600 PMTs arranged in a geodesic dome configuration having a 6 m radius. The PMTs detect Cherenkov light produced by relativistic electrons resulting from interactions with the heavy water by electron neutrinos. The unique use of heavy water as a neutrino target permitted SNO to make separate measurements of the flux of electron neutrinos and of the flux of all neutrino flavors. SNO was one of the earliest detectors that yielded information on all three electron, muon and tau neutrinos. Prior detectors were primarily sensitive only to electron neutrinos. The SNO detector is currently being upgraded for the new SNO+ experiments [23][24].

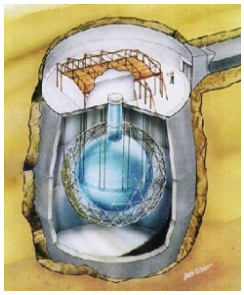

Figure 4 Sudbury Neutrino Detector [10].

### d. Monopole Astrophysics and Cosmic Ray Observatory (MACRO)

The Monopole Astrophysics and Cosmic Ray Observatory detector illustrated in Figure 5 and located in the Gran Sasso underground laboratory in Italy, was used to detect neutrinos from 1989 to 2000. It was originally constructed to search for the theoretical magnetic monopole and then,

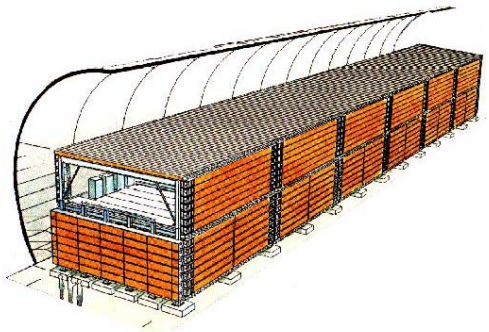

Figure 5 Illustration of the MACRO detector in Gran Sasso, Italy [25].

later, used in various neutrino studies. It contained stacked horizontal layers consisting of absorbers; liquid scintillator counters, weighing 600 tons; streamer tubes and nuclear track detectors. Liquid scintillator counters covered the outer top, bottom and sides. The streamer tubes were used for muon tracking and the scintillator counters were used for fast timing. The tracking precision was within 1 cm over several meters track length; the timing precision was within 600 ps (i.e. about 18 cm precision for a particle traveling near the speed of light). The detector volume was 8,550 cubic meters and it had an average rock overburden of 3700 hg/cm$^2$ that reduced the atmospheric muon flux by a factor of ~ $10^6$. Reducing the atmospheric muon flux facilitated measurements of muons produced by up-going neutrinos [5][26].

### e. Antarctic Muon and Neutrino Detector Array (AMANDA)

The Antarctic Muon and Neutrino Detector Array, illustrated in Figure 6, is a three dimensional array of PMTs located 1.5 to 2 km inside the Antarctic ice cap and completed in 2000. The array consists of 677 spherical optical sensors (~10 cm diameter) suspended by 19 strings of fiber-optic cables arranged in a cylinder 120 m in diameter and 500 m high. The enclosed volume is 4.3 x $10^6$ m$^3$ for the lower stage and 0.5 x $10^6$ m$^3$ for the upper stage for an overall volume of 4.8 x $10^6$ m$^3$. The PMTs are used to detect Cherenkov light pulses emitted by relativistic muons produced from cosmic neutrino interactions and propagating greater than the velocity of light in frozen water. AMANDA is being expanded to a larger volume of 1 km$^3$ that includes an array of eighty-six strings of light detectors along with radio antennas and renamed IceCube. This scaled up version is planned to operate as a neutrino telescope [16].

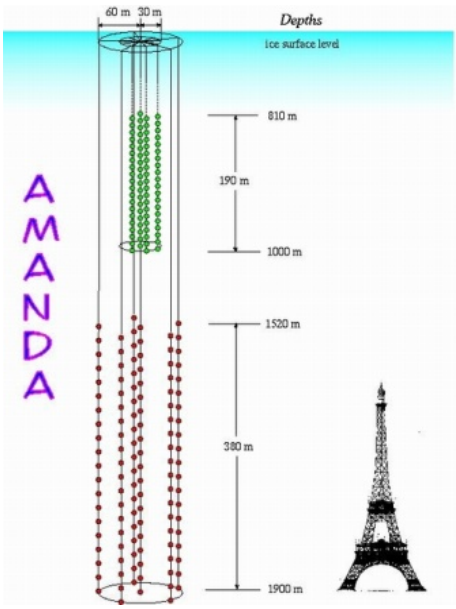

Figure 6. Antarctic Muon and Neutrino Detector Array [11].

## f. Pierre Auger Observatory

The Pierre Auger Observatory located south of Mendoza, Argentina, is primarily a cosmic ray detector but also is used for detecting high energy neutrinos. It consists of an array of 1600 small water tanks having a total volume of 30,000 $km^3$ and spread uniformly over a 3000 $km^2$ area. This area illustrated in the map shown in Figure 7 is about the size of the state of Rhode Island. It detects scintillation light and also Cherenkov light pulses both in the air and in the water tanks. It has an angular resolution of 0.5 to 2 degrees and has an energy range of $10^{17}$ to $10^{21}$ eV. In studying the direction of high energy cosmic rays, it was found that there is a strong association between cosmic ray source directions and AGN [3].

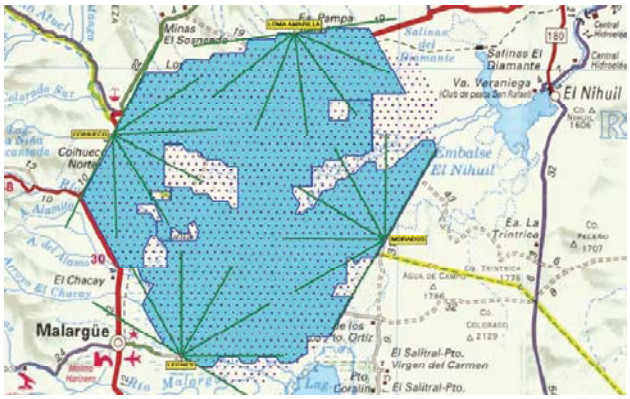


Figure 7 Map of the Pierre Auger Observatory [3].

## g. Astronomy with a Neutrino Telescope and Abyss environmental RE-Search (ANTARES)

The ANTARES detector is located in the Mediterranean Sea near Toulon, France. It consists of 900 PMTs positioned 2475 m underwater and positioned to detect Cherenkov light from particles produced by neutrino interactions. The PMTs are configured in a cylindrical arrangement of 12 lines each having 75 detectors and

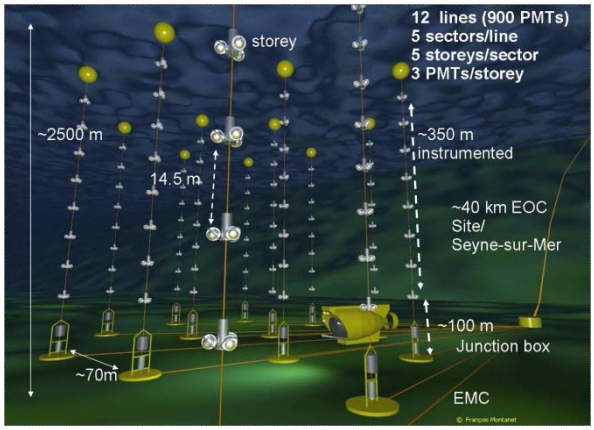


Figure 8. Illustration of ANTARES underwater neutrino detector located in the Mediterranean Sea [19].

covering a deep seabed of 0.06 $km^2$. High angular resolution can be achieved if the Cherenkov photons travelling in water are detected with an accuracy of 0.5 ns [19]. In an interim report for the ANTARES collaboration by Lambard (2008), the expected angular resolution for neutrino direction was expected to be 0.2 degrees for neutrinos having energies greater than 10 TeV. Figure 8 is an illustration showing the detectors attached to cables attached between floats and seabed anchors.

| **Detector** | **Location** | **Volume** | **Mass** | **Angular Resolution** | **Design** | **Date of Opertion** |
|---|---|---|---|---|---|---|
| Super-Kamiokande | North of Nagoya, Japan | 50,000 $m^3$ | 50 kT | 26 degrees [2] | Water absorber, detects Cherenkov radiation | 1996- |
| SNO | Sudbury, Ontario, Canada | 905 $m^3$ | 1 kT | | Heavy water absorber, detects Cherenkov radiation | 1999-2006 |
| MACRO | Gran Sasso, Italy | 8,550 $m^3$ | 600 T | 0.14˚ - 0.29˚ [25] | Liquid scintillators, trays of crushed rock, streamer tubes, and steel trays | 1989-2000 |
| AMANDA | Antarctica | 4.8 x $10^8$ $m^3$ | - | | Frozen water absorber, detects Cherenkov radiation | 2000- |
| Pierre Auger Observatory | South of Mendoza, Argentina | 30,000 $m^3$ | - | 0.5˚-2.0˚ [2] | Detects Cherenkov radiation in both air and in 1,600 small water tanks over a 3000 $km^2$ area | 2004- |
| ANTARES | Mediterranean Sea near Toulon, France | 50,000 $m^3$ | - | 0.3˚ [2] | Sea water absorber, detects Cherenkov radiation | 2008- |
| MINOS | Soudan, Minnesota | 1,530 $m^3$ | 11 kT | | Polystyrene plastic scintillators between 600 layers of magnetized steel plate absorbers | 2003- |

Table 1. Summary of neutrino detectors, locations and specifications.

## III. Prior Searches for AGN Neutrinos

There have been several studies conducted using these detectors in an attempt to find an association between point sources for high energy neutrinos and AGN. The Pierre Auger

Collaboration by Abraham et al. (9 November 2007) was able to establish a strong association between cosmic ray directions and nearby AGN. Of course, cosmic rays are attributed to high energy protons, not neutrinos. The authors reported that 12 events out of 15 having energies greater than 60 EeV were located to within 3.1˚ of AGN closer than 75 Mpc from Earth. If cosmic rays tend to be protons or nuclei, only sources closer than 200 Mpc from Earth can make an appreciable contribution to a measured flux above 60 EeV. Protons or nuclei above 60 EeV, unlike neutrinos, interact with the cosmic microwave background and, thereby, encounter strong flux attenuation from distant sources [13]. The authors noted that the catalog of AGN used in the study was incomplete near the galactic plane where the measurement sensitivity is reduced due to interactions with the Milky Way dust [15]. Thus, if high energy neutrinos originate from AGN like cosmic rays, one could expect that using neutrinos to find AGN point sources should result in significant improvement since neutrinos do not suffer flux attenuation like protons and nuclei from distant AGN or AGN located along the galactic plane. The neutrinos do present a different challenge in that they only have weak interactions and, therefore, are difficult to detect.

The AMANDA detector was used to search the northern sky by observing up-going muons at the Antarctica site for high energy neutrino point sources in a study performed in 1997 by Anders et al. In a sample of 1097 events their point source analysis essentially yielded a random distribution for energies greater than 1 TeV. The neutrino sources appear to be isotropically distributed over the northern sky. In other words, they were not able to demonstrate any high energy point sources clustered about AGN. The measured flux was consistent with most theoretical models that predict an approximate $E^{-2}$ energy spectrum for potential astrophysical sources of neutrinos [16]. It is worth noting that in an AMANDA study of nearly 500 Gamma-Ray Bursts by Kuehn (2005), no neutrino events were observed that could be directly associated with the bursts [18].
Thrane et al. (2009) performed a study over 2623 days from April 1996 to August 2007 to search for neutrino point sources by analyzing up-going muon data from the Super-Kamiokande detector. They searched for neutrino source clustering around candidate

galactic and extragalactic sources and transient sources. The study identified 16 plausible neutrino point source candidates. The search was limited to neutrinos having energies above 1.6 GeV. The authors reported interesting signatures for two sources, RX J1713.7-3946, a Super Nova Remnant, and GRB 991004D, a Gamma Ray Burst; however the data did not have "compelling statistical significance" [7]. This supports an earlier study at the same site reported by Abe et al. (2006) in which 2359 events of up-going muons were studied from April 1996 to July 2001 and no statistically significant evidence was found that could be linked to likely point sources [6]. Another study, using AMANDA-II data, Achterberg et al. (2006) did not identify any neutrino "hot spots" or any statistically significant neutrino point sources [29].

In a study conducted using the MACRO detector by Ambrosio et al. (2001), 1100 up-going muon events were observed from 1989 to 2000. The authors found no significant signal with respect to statistical fluctuations of the background due to atmospheric neutrions from any candidate AGN sources [26].

In a previous study using the Soudan 2 detector, DeMuth (1999) observed 44 events detecting high energy muons. The Soudan 2 detector was a forerunner of the MINOS detector and lacked the capability to distinguish between up-going and down-going muons [21]. While this study could not rule out AGN neutrino production models, it did not directly identify AGN as point sources of high energy neutrinos [22].
Thus, there have been prior studies at four neutrino detector sites. The studies attempted to determine whether high energy neutrino point sources could be attributed to known AGN. Finding neutrino point sources clustered in the vicinity of AGN would have demonstrated the connection. However, there was no compelling statistical connection made in any of the prior studies.

## IV. Active Galactic Nuclei

Thirty eight sources of Very High Energy (VHE) gamma rays were considered as likely sources of AGN high energy neutrinos. These were selected from the VHE catalogue maintained by the Max Planck Institut fur Physik. These are listed in Table 2 and shown in the VHE γ-ray Sky Map in galactic coordinates, Figure 9, available at http://www.mppmu.mpg.de/~wagner/sources/. The blazars indicated by dark red circles and a magenta circle, the three radio galaxies indicated by open crosses, one radio quasar indicated by an orange square, and the two starburst galaxies indicated by open squares were the AGN selected for this study.

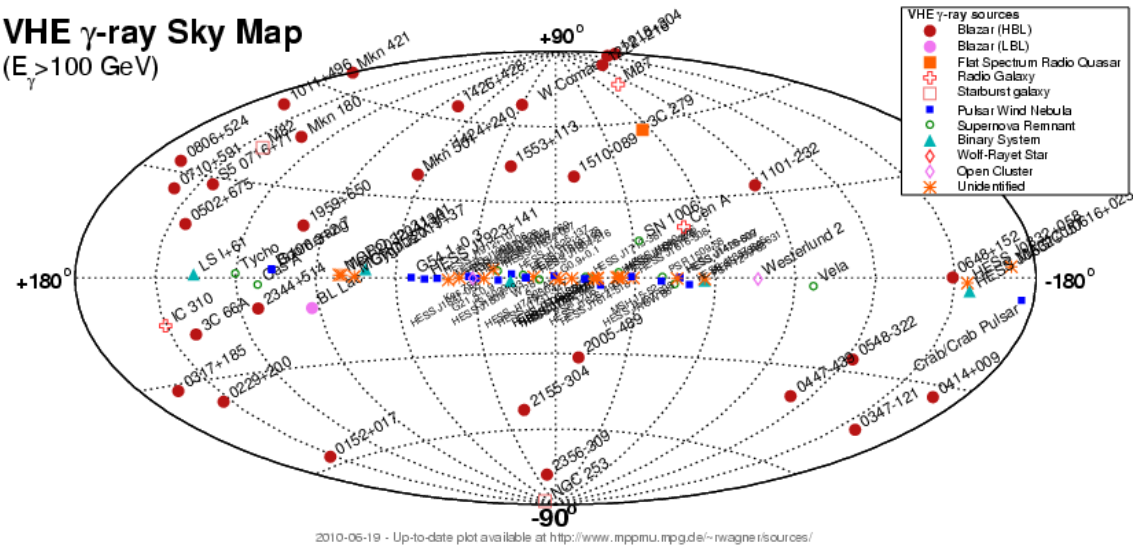


Figure 9. Very High Energy source γ-ray Sky Map in galactic coordinates.

| VHE Source | Right Ascension, deg | Declination, deg | Type |
|---|---|---|---|
| NGC 253 | 11.888042 | -25.288278 | Starburst Galaxy |
| RGB J0152+017 | 28.164958 | 1.788111 | Blazar (HBL) |
| 3C 66A | 35.665048 | 43.035500 | Blazar (HBL) |
| MAGIC J0223+430 | 35.797547 | 42.992051 | Blazar (HBL) |
| 1ES 0229+200 | 38.202500 | 20.288056 | Blazar (HBL) |
| IC 310 | 49.179500 | 41.324611 | Radio Galaxy |
| RBS 0413 | 49.965958 | 18.759694 | Blazar (HBL) |
| 1ES 0347-121 | 57.346667 | -11.990833 | Blazar (HBL) |
| 1ES 0414+009 | 64.218375 | 1.090083 | Blazar (HBL) |
| PKS 0447-439 | 72.352917 | -43.835833 | Blazar (HBL) |
| 1ES 0502+675 | 76.984583 | 67.623333 | Blazar (HBL) |
| VER J0521+211 | 80.479167 | 21.190000 | Blazar (HBL) |
| PKS 0548-322 | 87.669167 | -32.271222 | Blazar (HBL) |
| RGB 0648+152 | 102.198542 | 15.273556 | Blazar (HBL) |
| RGB J0710+591 | 107.625292 | 59.139028 | Blazar (HBL) |
| S5 0716+71 | 110.472702 | 71.343434 | Blazar (HBL) |
| 1ES 0806+524 | 122.454958 | 52.316222 | Blazar (HBL) |
| M82 | 148.967458 | 69.680222 | Starburst Galaxy |
| 1ES 1011+496 | 153.767375 | 49.433500 | Blazar (HBL) |
| 1ES 1101-232 | 165.906542 | -23.491722 | Blazar (HBL) |
| Mkn 421 | 166.113808 | 38.208833 | Blazar (HBL) |
| Mkn 180 | 174.110035 | 70.157585 | Blazar (HBL) |
| 1ES 1218+304 | 185.341417 | 30.176972 | Blazar (HBL) |
| W Comae | 185.382044 | 28.232917 | Blazar (HBL) |
| M87 | 187.705931 | 12.391123 | Radio Galaxy |
| 3C 279 | 194.046527 | -5.789312 | Radio Quasar |
| Centaurus A | 201.365063 | -43.019113 | Radio Galaxy |
| PKS 1424+240 | 216.751632 | 23.800010 | Blazar (HBL) |
| H 1426+428 | 217.135708 | 42.673556 | Blazar (HBL) |
| PKS 1510-089 | 228.210554 | -9.099953 | Blazar (HBL) |
| PG 1553+113 | 238.929350 | 11.190102 | Blazar (HBL) |
| Mkn 501 | 253.467569 | 39.760169 | Blazar (HBL) |
| ES 1959+650 | 299.999384 | 65.148515 1 | Blazar (HBL) |
| PKS 2005-489 | 302.355795 | -48.831589 | Blazar (HBL) |
| PKS 2155-304 | 329.716938 | -30.225588 | Blazar (HBL) |
| BL Lacertae | 330.680381 | 42.277772 | Blazar (LBL) |
| ES 2344+514 | 356.770496 | 51.704964 1 | Blazar (HBL) |
| H 2356-309 | 359.782958 | -30.628167 | Blazar (HBL) |

Table 2. Thirty eight Active Galactic Nuclei used in this study. The locations are given in equatorial coordinates along with the name and type.

Most of the AGN in Table 2 are blazars. A blazar is a very compact quasar presumed to be centered by a super massive black hole in a giant active galaxy. A blazar is surrounded by an accretion disk having particle jets perpendicular to the disk along the axis of rotation of the black hole. The jets form along magnetic fields produced by the rotation of charged particles in the accretion disk as shown in Figure 10. Blazars are difficult to detect at optical frequencies. Instead, nearly all of them have been detected and studied in the radio or X-ray band [17]. Blazars are a classification of Radio Loud AGN (RL-AGN) having jet beacons in the direction of observers. BL Lacertaes is the prototype for this class. There are two categories, defined by Padovani & Giommi (1995), as "Low-frequency peaked BL Lacs" (LBL) and "High-frequency BL Lacs" (HBL) which depend on whether the radio spectral index $\alpha_{rx}=\log(F_{5\ GHz}/F_{1\ keV})/7.68$ is greater than or less than 0.75, respectively. $F_{5\ GHz}$ and $F_{1\ keV}$ are frequency and energy flux values in Jansky (Jy) units, respectively. It is not certain whether there is a clear distinction between these categories or whether they are part of a continuous distribution [8]. AGNs characteristically have extreme variations in brightness.

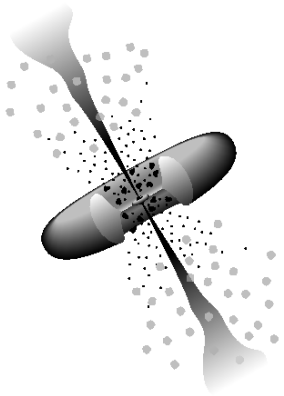

Figure 10. Model of an AGN with a luminous accretion disk. The disk surrounds a black hole and has two jets perpendicular to the axis of rotation [12].

These AGN are also shown again in a Mollweide projection in Figure 11 mapped in equatorial coordinates. The equatorial coordinate system based on the vernal equinox solar position and using the right ascension (RA) and declination (Dec) reference coordinates is the same system as used in the MINOS database and for this study.

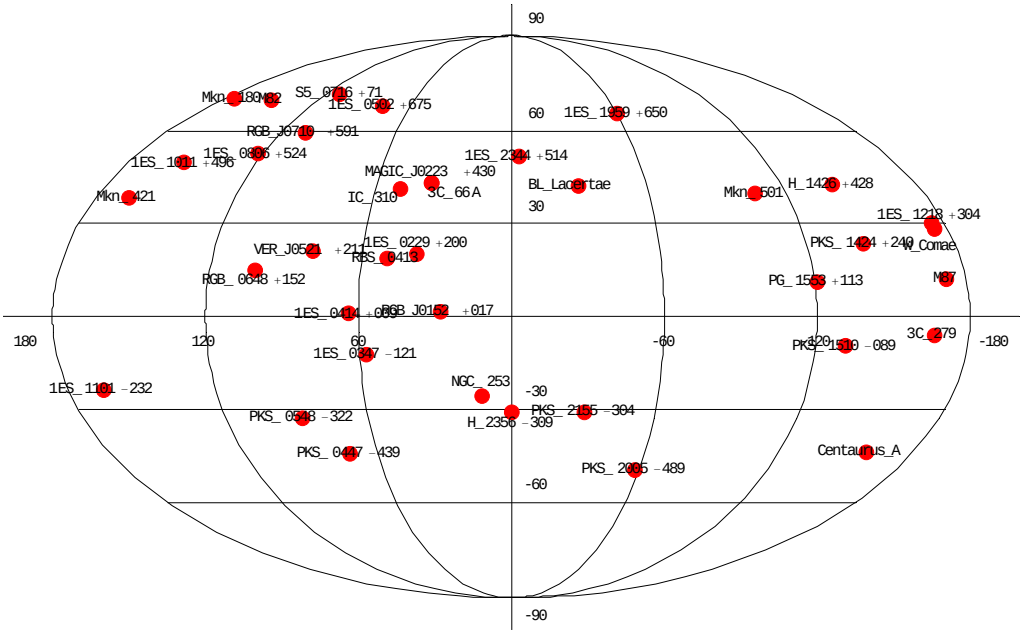


Figure 11. Mollweide projection of selected AGN in equatorial coordinates.

In attempting to analyze extragalactic neutrino sources, it is necessary to understand the placement and possible impact of potential high energy neutrino sources in the nearby Milky Way. Therefore, the equatorial coordinate celestial sky is illustrated again, in Figure 12, with the Milky Way galactic plane superimposed as a blue band. Star locations or approximate constellation centers, identified by solid blue circles from Table 3, were used to map the Milky Way plane in the figure.

| Star/Constellation | RA | Dec |
|---|---|---|
| Sirius | 101.29 | -16.72 |
| Betelgeuse | 88.79 | 7.41 |
| Algol | 47.042 | 40.96 |
| Altair | 297.70 | 8.87 |
| M6 | 265.08 | -32.20 |
| M103 | 23.35 | 60.65 |
| M1 | 83.63 | 22.01 |
| B Tau | 67.21 | 13.05 |
| M93 | 116.15 | -23.87 |
| center | 266.41 | -28.94 |
| M52 | 351.2 | 61.58 |
| M71 | 298.44 | 18.78 |
| M38 | 82.18 | 35.86 |
| Capella | 79.17 | 46.00 |
| M37 | 88.08 | 32.55 |
| M7 | 268.45 | -34.78 |
| CRUX | 180.00 | -63.0 |
| VELA | 150.00 | -55.0 |
| PUPPIS | 120.0 | -40.0 |
| CANIS MAJOR | 115.5 | -24.0 |
| ARA | 255.0 | -50.0 |
| MUSCA | 195.0 | -70.0 |
| CIRCINUS | 125.0 | -62.0 |
| Geminga | 98.48 | 17.77 |
| PERSEUS | 45.0 | 50.0 |

Table 3. Equatorial coordinates of the Milky Way stars and constellation reference points selected to plot an approximate Milky Way horizon.

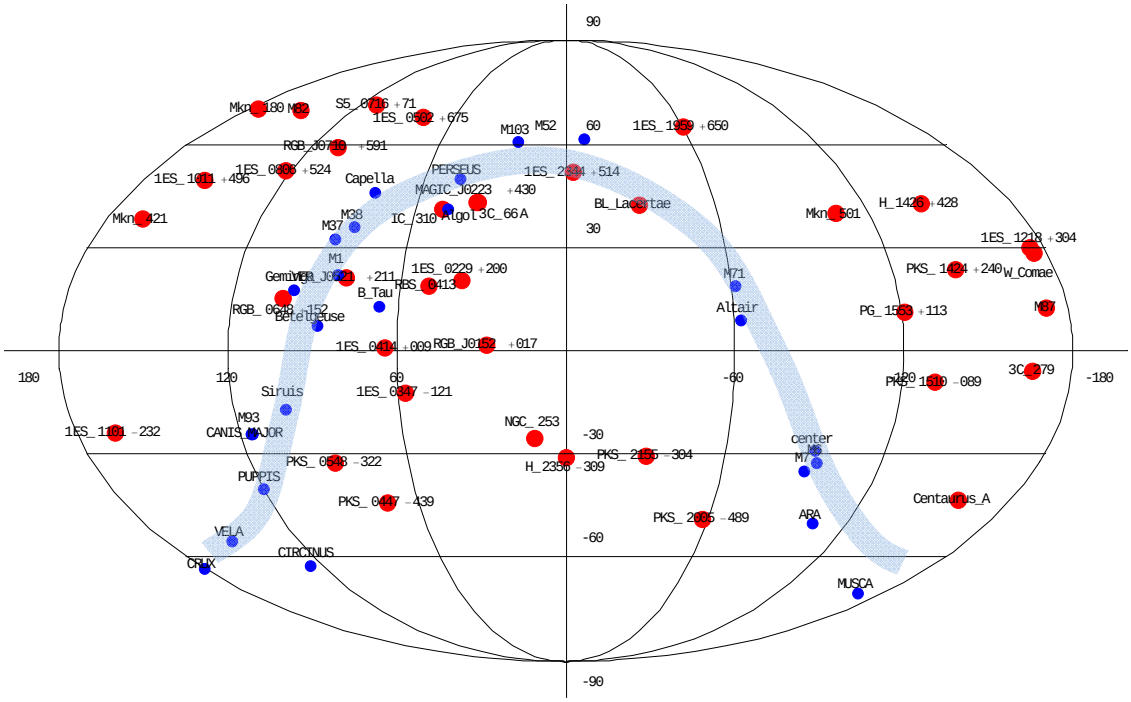


Figure 12. Mollweide sky map of AGN and the Milky Way plane in equatorial coordinates. The AGN are taken from Table 2 and selected reference objects used for the plane of the Milky Way are listed in Table 3. The approximate plane of the Milky Way is shown with the light blue band.

## V. Experimental Setup

Events occurring within the MINOS Far Detector are stored in the MINOS data file. The data file can be used to reconstruct muon tracks, determine muon momentum and energy, muon charge, and muon path and direction. The data file also can be queried to obtain the declination and right ascension coordinates of cosmic and up-going or horizontal muons.

For this study, a C++ program was written to query the database and select up-going muon events based on several criteria. Some of the more relevant selection criteria were the following:

1. Momentum ≥ 1GeV
2. Cos θ ≥ -0.1
3. Number of hits in track ≥ 12, used to ensure goodness of reconstructed track path
4. Chi-sqrd/no of hits ≤ 3.0, used to set limit on scatter of muon track data points
5. Time no digits ≥ 12, provides a means of determining up-going versus cosmic muons

Selecting the momentum to be greater than 1 GeV removed solar neutrinos from consideration. Selecting cos θ ≥ -0.1 permitted some muons slightly above horizontal to be included in the study. This was done to maximize the search field while still excluding cosmic generated muons from the data. The choice of the cos θ limit of -0.1 can be calculated by allowing for the Earth curvature and assuming that the maximum muon penetration in the bedrock surrounding the Soudan mine is approximately 6,500 m. This distance from the detector to the surface is shown as length B in Figure 13. The

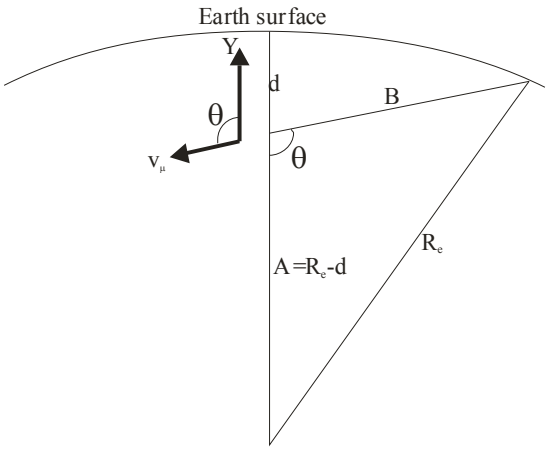


Figure 13. Vector analysis to set cos θ limit for horizontal neutrinos entering earth and traveling along B to detector located at distance d below ground.

depth of the detector is represented by d=666 m, making allowance for local elevation variations in the vicinity of the mine. The radius of the Earth, represented by $R_e$, is 6.366365 x $10^6$ m at 47˚ 49'13.29" N. Latitude and 92˚ 14' 31.23" W. Longitude, the location of the Soudan mine. The result cos θ = -0.1 is found by solving the equation $R_e^2 = A^2+B^2-2AB \cos \theta$. Vector representations for the detector vertical and the velocity of a muon, $v_\mu$, are shown in the diagram.

After the initial computer selection of candidate muon tracks was made, the reconstructed track images were visually sorted to eliminate obvious issues. For example, the software was not completely reliable in distinguishing between "up-going" and "down-going". The initial computer search was performed on MINOS data collected over a four-and-a-half year time period. There were 3486 muon events detected, or an average of 775 events per year, that met the initial computer criteria. These were the candidates that were visually scanned to eliminate events that had obvious issues such as multiple track events, poor track resolution, indeterminate track paths, and so forth. Table 4 summarizes the number of muon tracks for each year that passed visual scanning. These selected tracks are a small subset of all events recorded at the detector each of which is collected and stored as an individual data entry called a run having individual tracks or showers called snarls.

| Year | Up-going Muons | After Visual Scan | Snarl start | Snarl end |
|---|---|---|---|---|
| 2005 | 733 | 156 | 28544 | 33480 |
| 2006 | 669 | 152 | 33483 | 37102 |
| 2007 | 720 | 158 | 37185 | 40124 |
| 2008 | 797 | 120 | 40127 | 42645 |
| 2009 | 567 | 80 | 42648 | 45211 |
| Total | 3486 | 666 | | |

Table 4. Summary of up-going muon events per year that passed the initial criteria computer cuts and the number of those remaining after performing a visual scan.

The MINOS software has a user interface panel and an output display panel that shows various viewpoints of reconstructed muon track events. Figures 14 and 15 are pictures that show displays of the types of images that were used in this study. Figure 14 shows the user interface panel along with information on the run and snarl numbers. This panel

provides values for the charge versus momentum (q/p), momentum versus charge (p/q) and track energy in GeV obtained from the reconstructed track. Also, included in the top panel, are (1) two reconstructions of transverse views of a muon track along the Z-axis of the detector as recorded by successive U and V planes and (2) a user interface panel that provides some track analysis tools and also allows the user to step forward or back to view other successive events or to view separate instances for events with multiple tracks. Figure 15 shows an output display that consists of seven subpanels. It is a reconstruction of the muon track in an X-versus-Z view (top), a Y-versus-Z view (side), and a Y-versus-X view (north end). The transverse views are repeated along the right side in the bottom grouping. In the center bottom of the panel, there are two subpanels that relate time to the muon travel in the Y (up) and the Z (north south detector axis) directions. The Time-versus-Y panel provided useful information for visually scanning the muon track data to sort for the up-going muon criteria for this study.

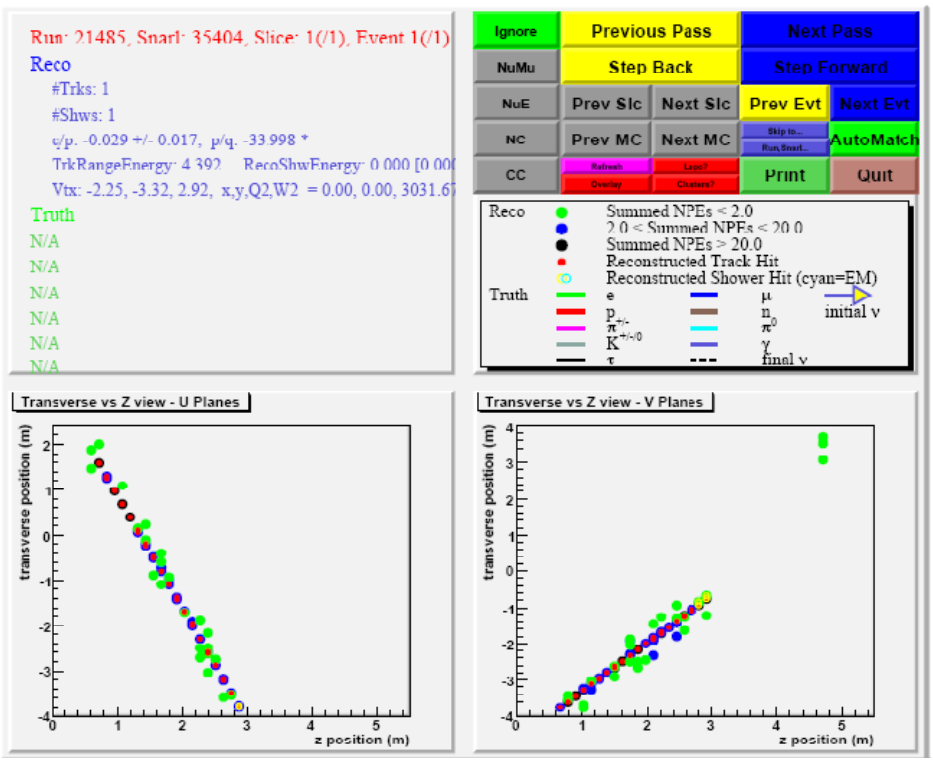


Figure 14. MINOS user interface display panel including muon track data and track reconstructions of the transverse U and V planes.

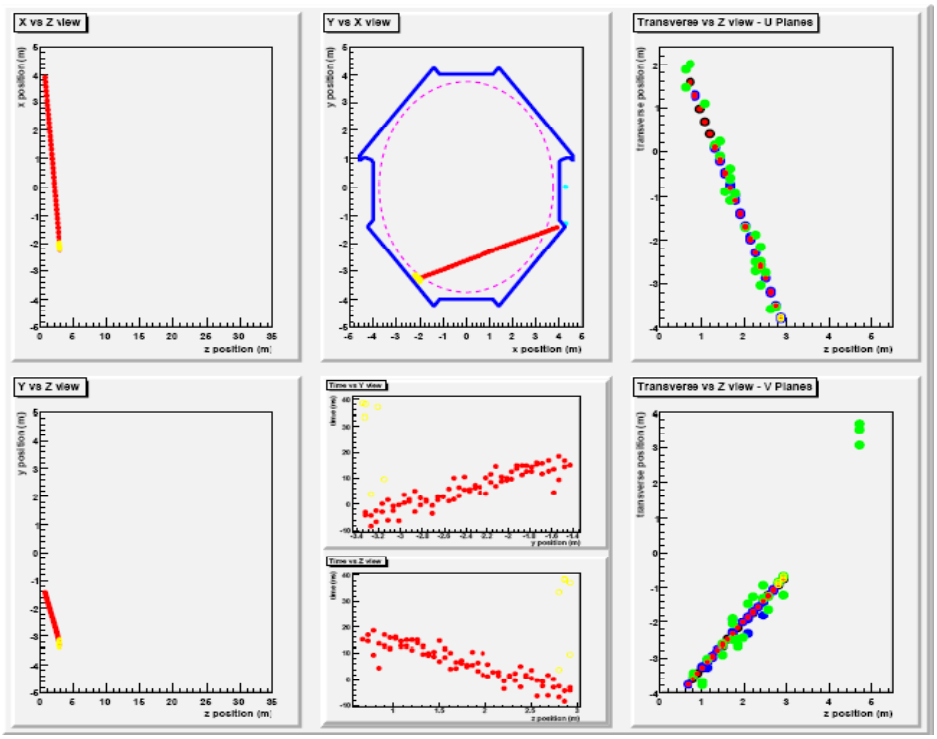


Figure 15. MINOS display panel of a muon track reconstruction. The top center panel has the outline of the MINOS detector traced in blue on the X-Y plane. Note that in the Time-vs-Y panel (top, lower center), the particle position (red dots) increases in the Y-direction with time. That is, it is moving up with respect to the detector. This is evident in the top center panel in which the particle enters from the lower left looking down the Z-axis of the detector (top center panel) and exits about one third up on the right of the detector.

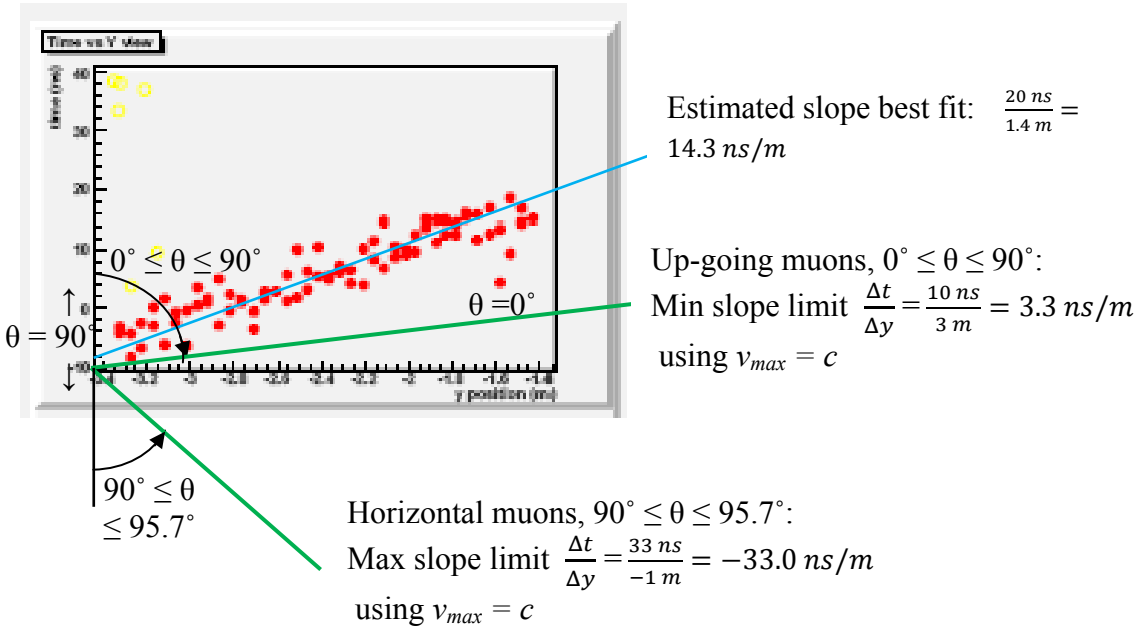


Figure 16. Time-vs-vertical distance display of a reconstructed up-going muon track and limits used for visual sorting.

The reconstructed muon track files produced by the MINOS software were visually scanned using the criteria of "up-going" tracks, scatter, single-muon event, and slope limits. The Time-vs-Y-View in Figure 16 illustrates a typical up-going muon track that met the visual selection criteria. Time, in ns units, is shown in the vertical direction and the distance traveled in the upward direction is shown on the horizontal scale in m units. The discrete muon hits, recorded by the detector, show up as red dots. The velocity of light in a vacuum is used as an approximation for the minimum Time-vs-Y of a muon traveling perpendicular to the detector. This is used to establish the minimum slope for $\frac{\Delta t}{\Delta y} = 3.3$ ns/m as shown in the figure for $0^\circ \leq \theta \leq 90^\circ$. Slopes within this range are accepted as illustrated by the scatter track. Also, since the horizontal-going muons are accepted for $\cos\theta \geq -0.1$, there is another slope, $\frac{\Delta t}{\Delta y} = 3.3$ ns/m, corresponding to an angle range of $90^\circ \leq \theta \leq 95.7^\circ$, as shown.

After doing visual analysis of the muon tracks, the data was sorted again based on the amount of error in the angle of incidence. The MINOS software outputs information on muon incident direction as a value of $\cos\theta$ with respect to the vertical. It also provides the right ascension and declination for the equatorial coordinate system and the error, $\Delta\cos\theta$. The error value that is needed however is $\Delta\theta$, not $\Delta\cos\theta$. An error of $\Delta\theta = 3^\circ$ was selected as a first cut value that seemed reasonable for describing a point source event occurring in the neighborhood of a celestial object like AGN. Therefore, the error values, $\Delta x = \Delta\cos\theta$, were sorted to obtain a constant error with respect to angle, $\Delta\theta$, by differentiating

$\cos^{-1}x = \theta$

to obtain $d\theta = \frac{-dx}{\sqrt{1-x^2}} \Rightarrow \Delta x = \sqrt{1-x^2}\,\Delta\theta$

The candidate up-going muons resulted from neutrino interactions in either the rock formations surrounding the MINOS detector or interactions within the detector itself. The energy distribution tally for the case $\Delta\theta = 3^\circ$ is shown in the first two columns of Table 5 and plotted in Figure 17 in log-log scale.

| Energy, GeV | Number, N $\Delta\theta = \pm 3^{\circ}$ | Flux, $\varphi_{\nu\mu}(E)$, $s^{-1}$ sr $cm^{-2}$ | Number, N $\Delta\theta = \pm 6^{\circ}$ | Flux, $\varphi_{\nu\mu}(E)$, $s^{-1}$ sr $cm^{-2}$ |
|---|---|---|---|---|
| 1 | 205 | 1.641 x $10^{-14}$ | 303 | 2.426 x $10^{-14}$ |
| 3 | 147 | 1.177 x$10^{-14}$ | 157 | 1.257x $10^{-14}$ |
| 10 | 113 | 9.048 x$10^{-15}$ | 116 | 9.288 x $10^{-15}$ |
| 30 | 97 | 7.767 x$10^{-15}$ | 98 | 7.847 x $10^{-15}$ |
| 100 | 45 | 3.603 x$10^{-15}$ | 45 | 3.603 x$10^{-15}$ |
| 300 | 26 | 2.082 x$10^{-15}$ | 26 | 2.082 x$10^{-15}$ |
| 1000 | 6 | 4.804 x$10^{-16}$ | 6 | 4.804x$10^{-16}$ |
| 3000 | 5 | 4.003 x$10^{-16}$ | 5 | 4.003 x$10^{-16}$ |
| Total | 644 | 5.156 x$10^{-14}$ | 756 | 6.053 x$10^{-14}$ |

Table 5. Distribution of muon energies with $\Delta\theta = \pm 3^{\circ}$ and $\Delta\theta = \pm 6^{\circ}$.

The generally accepted cosmic neutrino energy distribution has the form $\frac{dN}{dE} \alpha\, E^{-3.7}$. Figure 17 is a log-log plot of N versus E in which the count in each bin has been normalized to the bin energy width. Analysis of the plot suggests an equation of the form $y = ax^b$ having the nominal value b = -1.5. Thus, the neutrino count is found to falls off with increasing energy as follows:

$$N = cE^{-1.5}$$

$$dN = -1.52cE^{-2.5}dE$$

$$\frac{dN}{dE} \propto E^{-2.5}$$

Similarly, the log-log plot of the normalized neutrino flux, φ, versus energy, E, is shown in Figure 18. Again, the estimated neutrino flux falls off with increasing energy according to $\frac{d\varphi}{dE} \propto E^{-2.5}$.

Atmospheric neutrino flux falls off according to $\boldsymbol{\frac{d\varphi}{dE} \propto E^{-3.7}}$. However, point-source neutrino flux is thought to fall off according to $\boldsymbol{\frac{d\varphi}{dE} \propto E^{-2}}$ as reported in Thrane, et al [7] and Braun, et al [1]. It is significant therefore that the flux falls off proportional to $\boldsymbol{E^{-2.5}}$, found in the present study, is within the range of the Thrane and Braun studies.

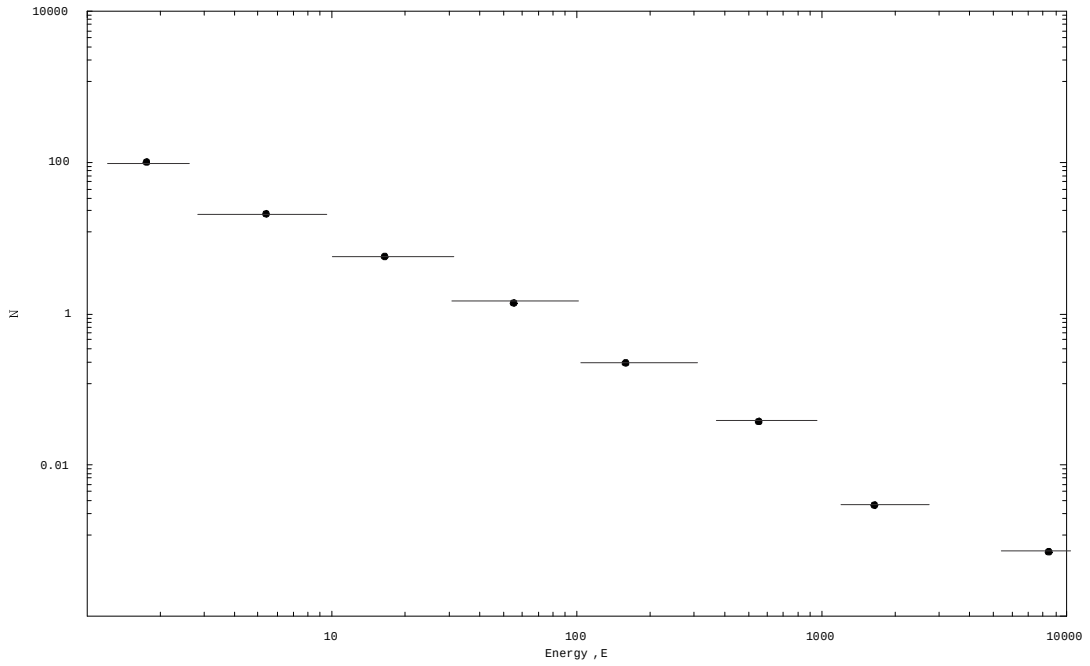


Figure 17. Log-log plot of muon energy distribution. Data from Table 5 was used for the case $\Delta\theta = \pm 3^{\circ}$. Interpreting the log-log slope leads to the approximate relationship $\frac{dN}{dE} \propto E^{-2.5}$

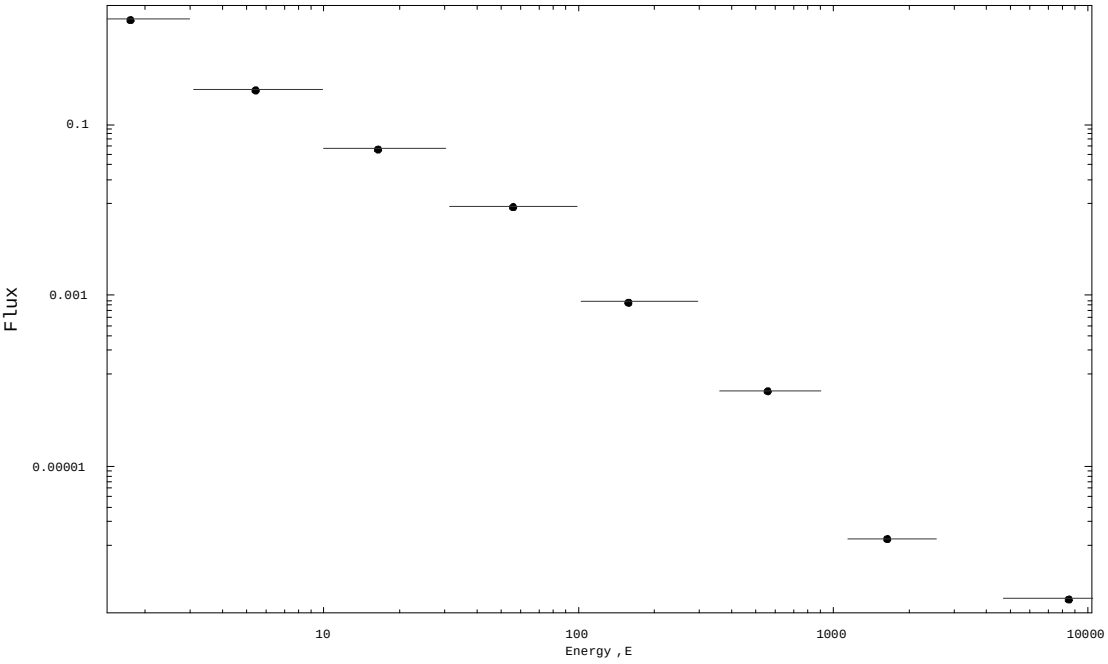


Figure 18. Log-log plot of muon flux distribution. Data from Table 5 was used for the case $\Delta\theta = \pm 3^{\circ}$. Interpreting the log-log slope leads to the approximate relationship $\frac{d\varphi}{dE} \propto E^{-2.5}$

## VI. Up-going Muon Flux

The up-going muon flux, $\varphi_{\mu\nu}$, at the MINOS detector, with the angular error $\Delta\theta = \pm 3^{\circ}$, can be estimated as follows:

$$\varphi_{\mu\nu} = \frac{dN}{dtdAd\Omega},$$

where $dN$=644, $dt$ = 4.5 y = 1.42 x $10^8$ s, $dA$ = 7.76 x $10^6$ $cm^2$, the outside area of the MINOS detector exposed to up-going muons, $d\Omega$ = 11.334 sr, the solid angle of the celestial sphere scanned by the MINOS detector calculated from $\Omega_\theta = 2\pi(1-\cos\theta)$ using the following:

- the MINOS detector location is 47.8˚ north latitude
- up-going muon data is used to a maximum of 5.7˚ above the horizon ($\cos\theta \geq -0.1$)
- $\theta = 90^{\circ}+47.8^{\circ}+5.7^{\circ}=143.5^{\circ}$, the subtended cone of the muon data collected

For the MINOS detector, the full energy range of muon flux is $\varphi_{\mu\nu}$ = 5.156 x $10^{-14}s^{-1}$ sr $cm^2$ with an angular error tolerance of $\Delta\theta = \pm 3^{\circ}$ and $\varphi_{\mu\nu}$ = 6.053 x $10^{-14}s^{-1}$ sr $cm^2$ at with an angular error tolerance of $\Delta\theta = \pm 6^{\circ}$. These values are lower but within one order of magnitude of the value of $\varphi_{\mu\nu}$ = 4.01 x $10^{-13}s^{-1}$ sr $cm^2$ obtained in a search for AGN neutrinos by DeMuth (2003) at Soudan 2, an earlier underground neutrino detector located at the same site as MINOS [27]. This is expected since the Soudan 2 detector did not have the capability to determine the muon angle of incidence unlike the MINOS detector. In the current study, data having angle of incidence errors that exceeded tolerance limits was discarded thereby reducing the total flux. Table 5 shows the total flux values along with flux values for intermediate energy values from 1 GeV up to 3 TeV and beyond for both cases, $\Delta\theta = \pm 3^{\circ}$ and $\Delta\theta = \pm 6^{\circ}$. This is plotted in Figure 19. Notice that for 100 GeV and above, the flux values appear to coincide for both angular error ranges.

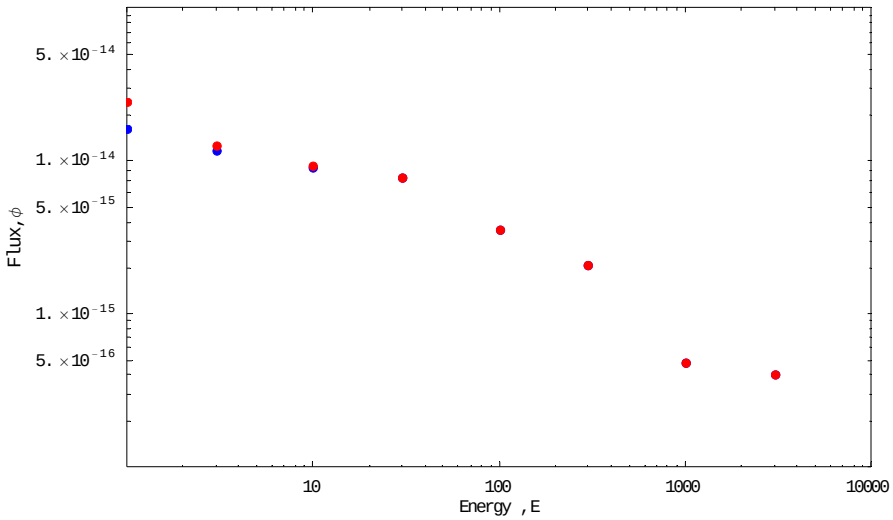


Figure 19. Flux vs Energy Plot. The case for $\Delta\theta = \pm 3^{\circ}$ is shown in blue and $\Delta\theta = \pm 6^{\circ}$ is shown in red.

## VII. Analysis

Using the MINOS data analysis software, the right ascension and declination were plotted on Mollweide equatorial coordinate celestial sky maps along with the 38 AGN identified earlier. Celestial sky maps for energy cuts at 1 GeV, 10 GeV, 100 GeV, 1000 GeV and 3000 GeV are shown in Figures 20-27. The celestial sky map of neutrino sources having 1 GeV or greater energy also includes a blue band to identify the relative position of the Milky Way horizon. The hypothesis that AGN are point sources for high energy neutrinos was tested by analyzing the sky plots to see whether neutrino sources were clustered around AGN. The sky map in Figure 20, based on a 3˚subtended angle of incidence error, has 644 hits. There are 26 AGN in the 11.334 sr scan field of data used for this study. So, there are, on average, 56.82 hits per sr expected. For a 3˚subtended angle of incidence error, the solid angle $\Omega_{\theta=3} = 0.00861$ sr. Therefore, if an AGN had no influence on neutrino origination, the average number of hits around an AGN with solid angle $\Omega_{\theta=3}$ would be 56.82 hits $sr^{-1}$ x 0.00861 sr = 0.4892 hits. The twenty-six AGN sites then should produce on average 26 x 0.4892 hits = 12.7 hits if there were no additional contributions from neutrinos produced by the AGN. Analysis of the Figure 20 sky map shows that there were 11 hits spread over 8 AGN (18 AGN sites were empty). Thus, the

total number of hits within all the AGN angular tolerance bands was no greater than an average expectation.

However, a more careful analysis that accounts for the relative time that a region of the celestial sky is within the detection region. This is done by breaking the equatorial sky plot into equatorial bands. This is done in 30˚ declinations starting at -90˚ up to +53.5˚ (stopping short of +60˚ due to the cutoff limit used for this study). Tables 7 through 12 contain a tabulation of the results for the cases $\Delta\theta = \pm 3^{\circ}$ and $\Delta\theta = \pm 6^{\circ}$ and energy steps in decades from ≥1 GeV to ≥100 GeV. A comparison of the columns labeled "Hits per sr" and "Hits per AGN sr" is a comparison of the average hits per sr in the declination band and the average hits per sr of all the AGN in the same band. There was only one instance in the 6 tables in which the average hits of the AGN sr exceeded the average hits per sr in the region. This occurred in Table 6 in the declination band -30˚ to 0˚ which shows 69.69 hits per AGN sr versus 53.47 hits per sr band average. This is only 30.3% more than expected and only occurs in only one of the twenty-four bands tabulated.
It is worth noting that the AGN identified by 1ES 0414+009 recorded 4 hits at energy ≥10 GeV for $\Delta\theta = \pm 6^{\circ}$, 3.5 more than the average. However, at higher energies, where the case for AGN originated neutrinos should be stronger, there were no hits observed.

| | $\Delta\theta = \pm 3^{\circ}$ | | | | | $\Delta\theta = \pm 6^{\circ}$ | | | | |
|---|---|---|---|---|---|---|---|---|---|---|
| Energy GeV | Number of hits | Hits/ sr | Hits/ AGN | Expected total hits | Actual total hits | Number of hits | Hits/sr | Hits/ AGN | Expected total hits | Actual total hits |
| 1 | 644 | 56.82 | 0.49 | 17.1 | 11 | 756 | 66.70 | 1.15 | 40.2 | 38 |
| 10 | 292 | 25.76 | 0.22 | 7.8 | 5 | 296 | 26.12 | 0.45 | 15.7 | 17 |
| 100 | 82 | 7.23 | .06 | 2.2 | 2 | 82 | 7.23 | 0.12 | 4.4 | 5 |
| 1000 | 11 | 0.97 | .01 | 0.3 | 0 | 11 | 0.97 | 0.02 | 0.6 | |
| 3000 | 5 | .44 | .00 | 0.1 | 0 | 5 | 0.44 | 0.01 | 0.3 | |

Table 6. Summary of measured neutrino sources in the vicinity of AGN.

| Energy ≥ 1 GeV and Δθ = ±3˚ | | | | | | | |
|---|---|---|---|---|---|---|---|
| Declination range, deg | Range sr | Number of hits | Hits per sr | Number of AGN | AGN per sr | AGN hits | Hits per AGN sr |
| 30 to 53.5 | 1.909 | 50 | 26.19 | 7 | 0.060 | 1 | 16.59 |
| 0 to 30 | 3.142 | 170 | 54.11 | 10 | 0.086 | 4 | 46.46 |
| -30 to 0 | 3.142 | 168 | 53.47 | 5 | 0.043 | 3 | 69.69 |
| -60 to -30 | 2.300 | 186 | 80.87 | 6 | 0.052 | 2 | 38.71 |
| -90 to -60 | 0.842 | 70 | 83.14 | 0 | 0.000 | 0 | |
| Totals: | 11.335 | 644 | | 28 | | 10 | |

Table 7. Summary of all muon hits having E ≥ 1 GeV and those having incident directions within 3˚error tolerance of AGN.

| Energy ≥ 10 GeV and Δθ = ±3˚ | | | | | | | |
|---|---|---|---|---|---|---|---|
| Declination range, deg | Range sr | Number of hits | Hits per sr | Number of AGN | AGN per sr | AGN hits | Hits per AGN sr |
| 30 to 53.5 | 1.909 | 24 | 12.57 | 7 | 0.060 | 1 | 16.59 |
| 0 to 30 | 3.142 | 76 | 24.19 | 10 | 0.086 | 2 | 23.23 |
| -30 to 0 | 3.142 | 80 | 25.46 | 5 | 0.043 | 1 | 23.23 |
| -60 to -30 | 2.300 | 81 | 35.22 | 6 | 0.052 | 2 | 38.71 |
| -90 to -60 | 0.842 | 31 | 36.82 | 0 | 0.000 | 0 | |
| Totals: | 11.335 | 292 | | 28 | | 6 | |

Table 8. Summary of all muon hits having E ≥ 10 GeV and those having incident directions within 3˚error tolerance of AGN.

| Energy ≥ 100 GeV and Δθ = ±3˚ | | | | | | | |
|---|---|---|---|---|---|---|---|
| Declination range, deg | Range sr | Number of hits | Hits per sr | Number of AGN | AGN per sr | AGN hits | Hits per AGN sr |
| 30 to 53.5 | 1.909 | 5 | 2.62 | 7 | 0.060 | 0 | 0.00 |
| 0 to 30 | 3.142 | 25 | 7.96 | 10 | 0.086 | 1 | 11.61 |
| -30 to 0 | 3.142 | 23 | 7.32 | 5 | 0.043 | 0 | 0.00 |
| -60 to -30 | 2.300 | 24 | 10.43 | 6 | 0.052 | 0 | 0.00 |
| -90 to -60 | 0.842 | 5 | 5.94 | 0 | 0.000 | 0 | |
| Totals: | 11.335 | 82 | | 28 | | | |

Table 9. Summary of all muon hits having E ≥ 100 GeV and those having incident directions within 3˚error tolerance of AGN.

| Energy ≥ 1 GeV and Δθ = ±6˚ | | | | | | | |
|---|---|---|---|---|---|---|---|
| Declination range, deg | Range sr | Number of hits | Hits per sr | Number of AGN | AGN per sr | AGN hits | Hits per AGN sr |
| 30 to 53.5 | 1.909 | 55 | 28.81 | 7 | 0.060 | 7 | 29.07 |
| 0 to 30 | 3.142 | 195 | 62.06 | 10 | 0.086 | 15 | 43.60 |
| -30 to 0 | 3.142 | 194 | 61.74 | 5 | 0.043 | 8 | 46.51 |
| -60 to -30 | 2.300 | 212 | 92.17 | 6 | 0.052 | 9 | 43.60 |
| -90 to -60 | 0.842 | 100 | 118.76 | 0 | 0.000 | 0 | |
| Totals: | 11.335 | | | 28 | | 39 | |

Table 10. Summary of all muon hits having E ≥ 1 GeV and those having incident directions within 6˚error tolerance of AGN.

| Energy ≥ 10 GeV and Δθ = ±6˚ | | | | | | | |
|---|---|---|---|---|---|---|---|
| Declination range, deg | Range sr | Number of hits | Hits per sr | Number of AGN | AGN per sr | AGN hits | Hits per AGN sr |
| 30 to 53.5 | 1.909 | 24 | 12.57 | 7 | 0.060 | 4 | 16.61 |
| 0 to 30 | 3.142 | 76 | 24.19 | 10 | 0.086 | 8 | 23.26 |
| -30 to 0 | 3.142 | 84 | 26.73 | 5 | 0.043 | 3 | 17.44 |
| -60 to -30 | 2.300 | 78 | 33.91 | 6 | 0.052 | 4 | 19.38 |
| -90 to -60 | 0.842 | 34 | 40.38 | 0 | 0.000 | 0 | |
| Totals: | 11.335 | 296 | | 28 | | 19 | |

Table 11. Summary of all muon hits having E ≥ 10 GeV and those having incident directions within 6˚error tolerance of AGN.

| Energy ≥ 100 GeV and Δθ = ±6˚ | | | | | | | |
|---|---|---|---|---|---|---|---|
| Declination range, deg | Range sr | Number of hits | Hits per sr | Number of AGN | AGN per sr | AGN hits | Hits per AGN sr |
| 30 to 53.5 | 1.909 | 5 | 2.62 | 7 | 0.060 | 1 | 4.15 |
| 0 to 30 | 3.142 | 25 | 7.96 | 10 | 0.086 | 2 | 5.81 |
| -30 to 0 | 3.142 | 22 | 7.00 | 5 | 0.043 | 1 | 5.81 |
| -60 to -30 | 2.300 | 25 | 10.87 | 6 | 0.052 | 1 | 4.84 |
| -90 to -60 | 0.842 | 5 | 5.94 | 0 | 0.000 | 0 | |
| Totals: | 11.335 | 82 | | 28 | | | |

Table 12. Summary of all muon hits having E ≥ 100 GeV and those having incident directions within 6˚error tolerance of AGN.

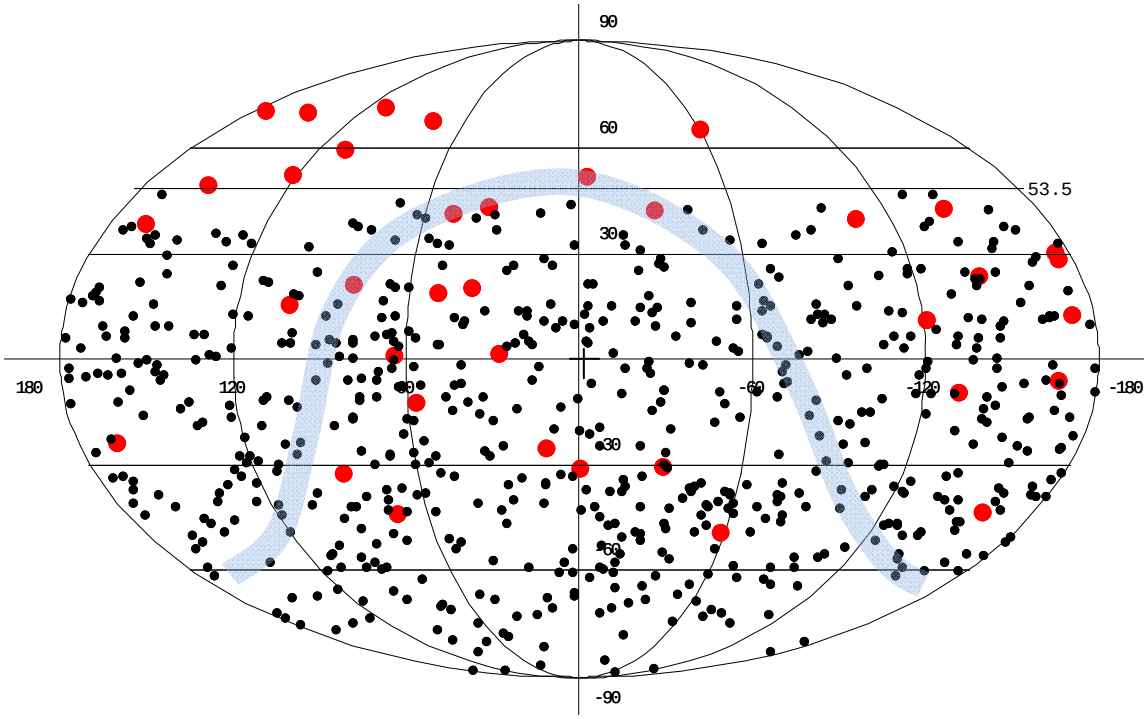


Figure 20. Equatorial coordinate sky map of AGN (red dots), neutrino sources having energy ≥ 1 GeV and angular error ≤ 3˚(black dots), and approximate horizon of the Milky Way (light blue band). The diameter of the red circles represent a 6˚error range around the AGN ( ±3˚error results in a 6˚ diameter error circle). The location of the MINOS detector at 47.8˚north latitude along with a 5.7˚ above horizontal view from the detector plane limits the effective neutrino hits to below 53.5˚ down to -90˚right declination. Notice that this eliminates 9 AGN above 53.5˚ declination from the study.

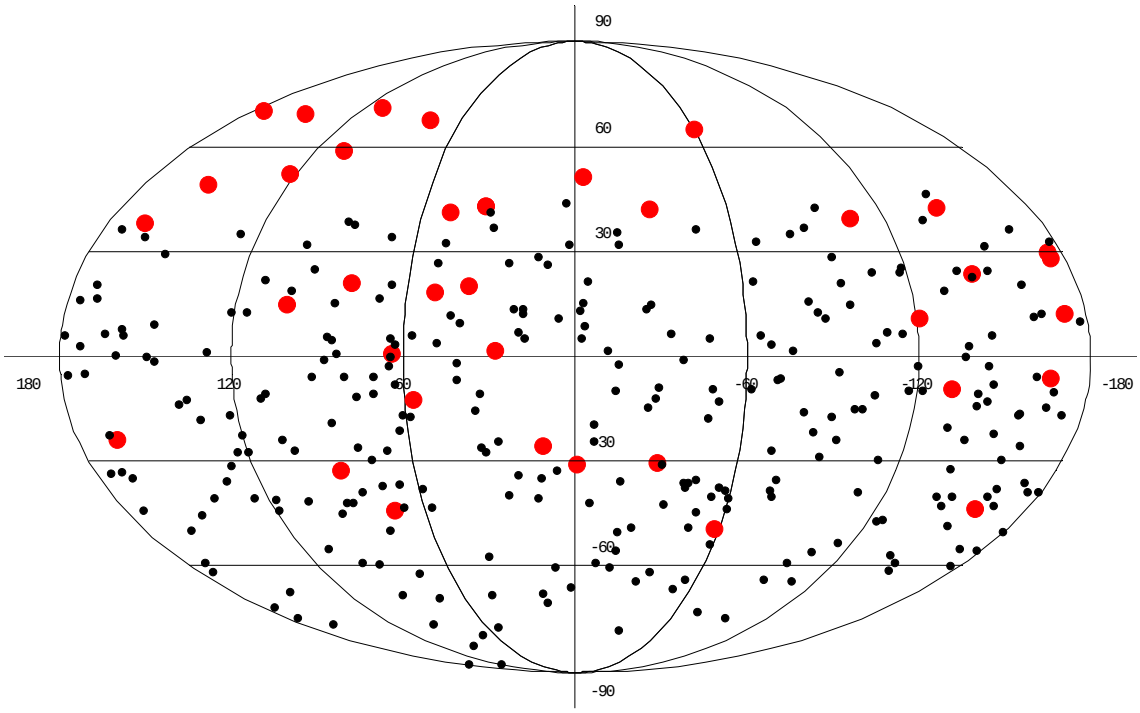


Figure 21. Sky map of AGN (red dots) and neutrino sources having energy ≥ 10 GeV and angular error ≤ 3˚. The diameter of the red circles approximately represents a 6˚error band around the AGN.

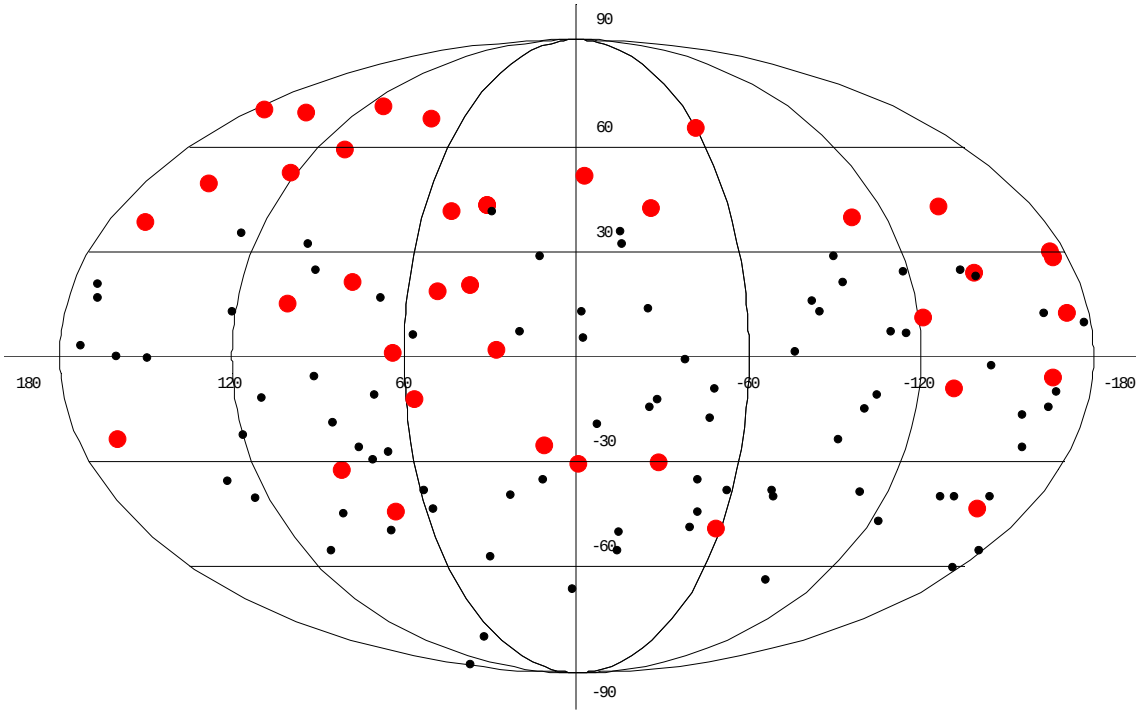


Figure 22. Sky map of AGN (red dots) and neutrino sources having energy ≥ 100 GeV and angular error ≤ 3˚. The diameter of the red circles approximately represents a 6˚ error band around the AGN.

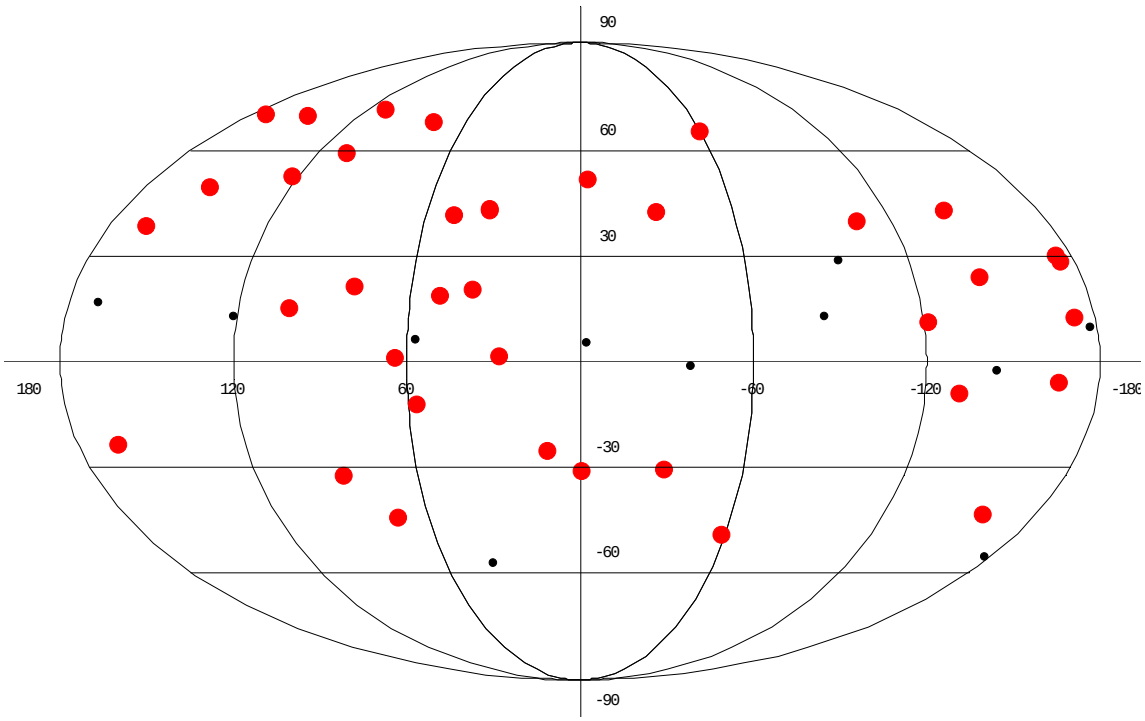


Figure 23. Sky map of AGN (red dots) and neutrino sources having energy ≥ 1000 GeV and angular error ≤ 3˚. The diameter of the red circles approximately represents a 6˚error band around the AGN.

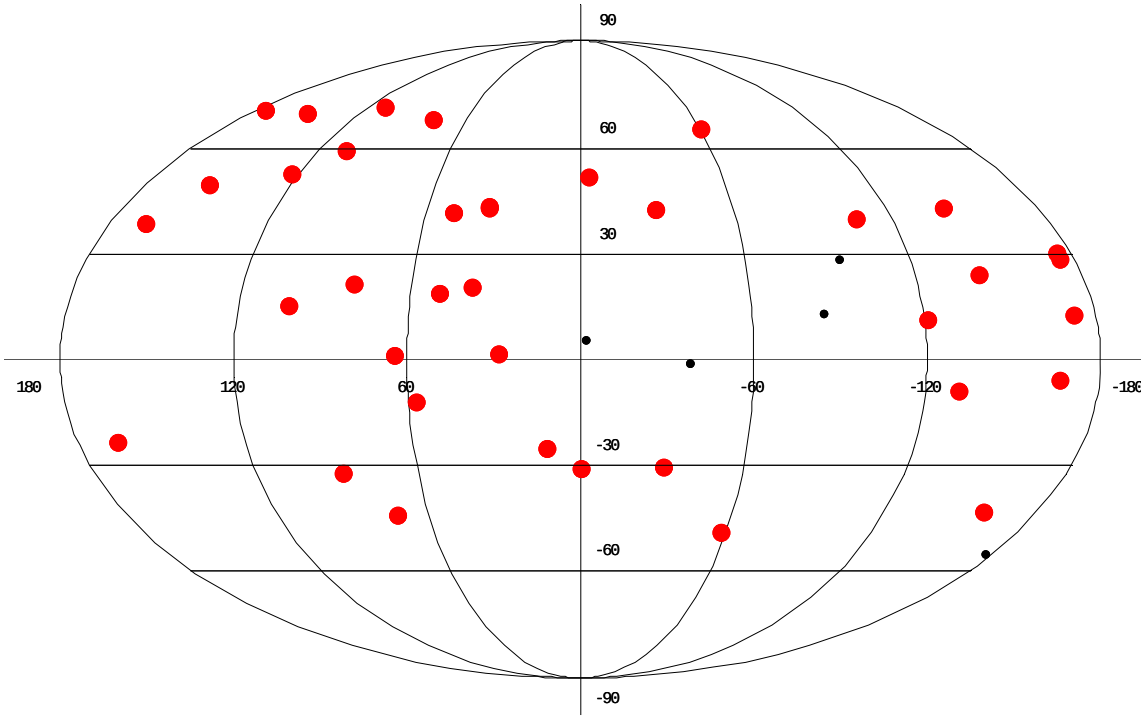


Figure 24. Sky map of AGN (red dots) and neutrino sources having energy ≥ 3000 GeV and angular error ≤ 3˚. The diameter of the red circles approximately represents a 6˚error band around the AGN.

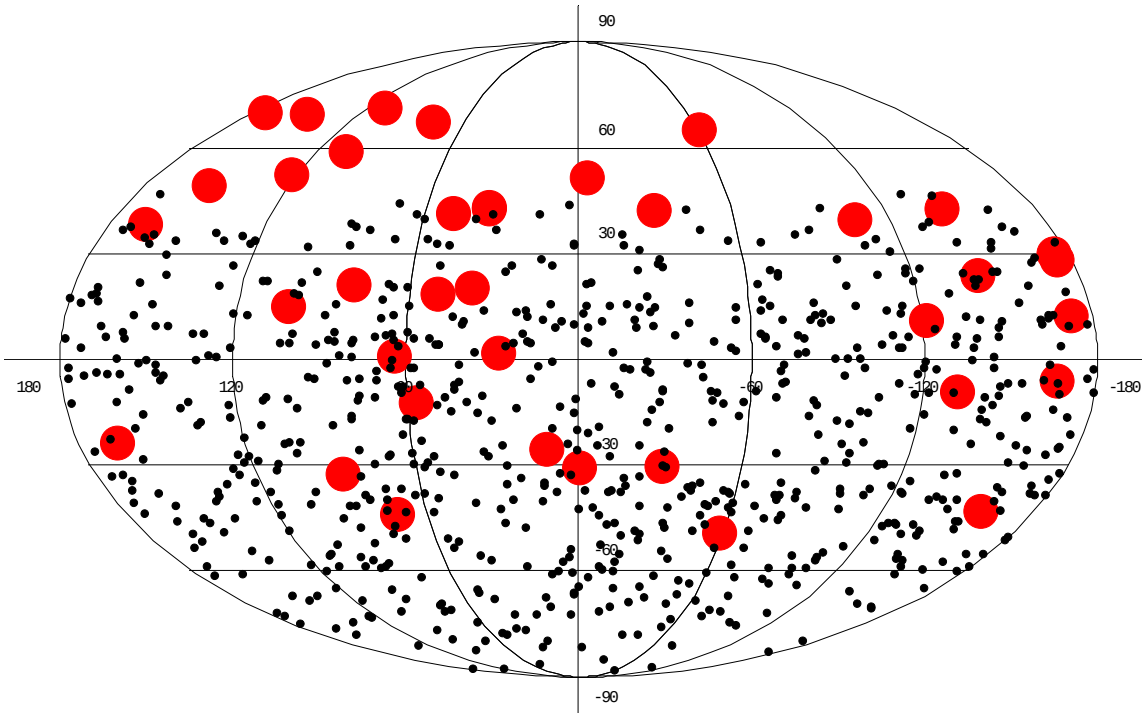


Figure 25. Sky map of AGN (red dots) and neutrino sources having energy ≥ 1 GeV and angular error ≤ 6˚. The diameter of the red circles approximately represents a 12˚error band around the AGN.

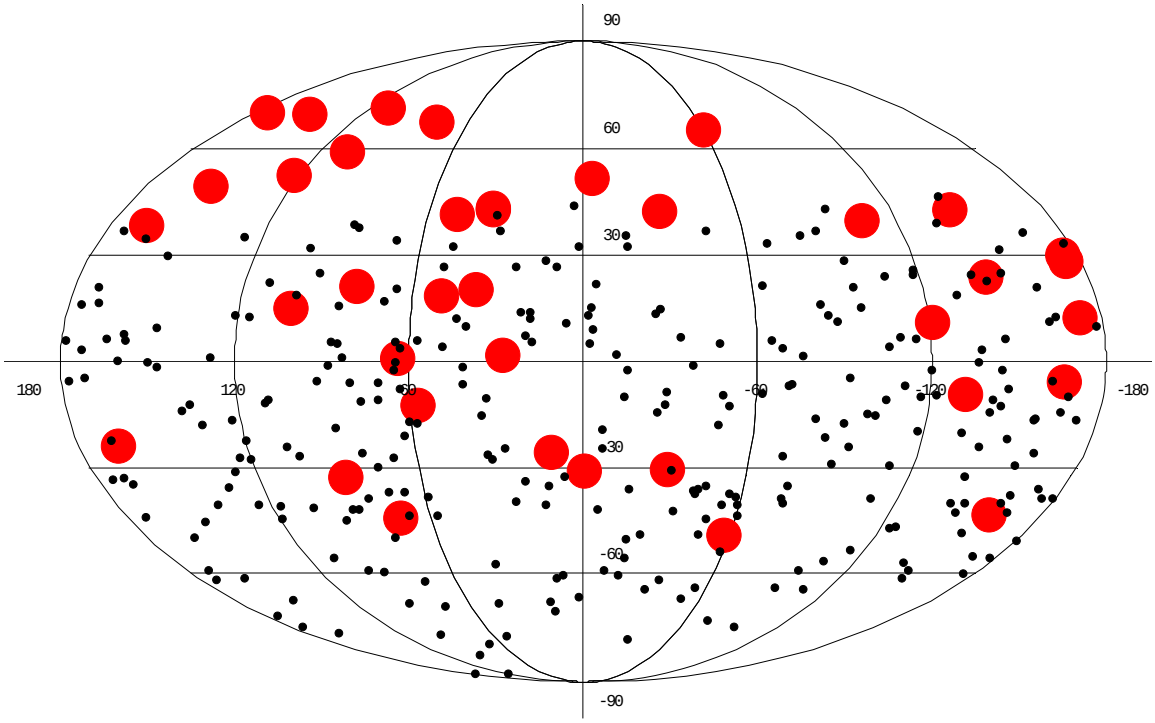


Figure 26. Sky map of AGN (red dots) and neutrino sources having energy ≥ 10 GeV and angular error ≤ 6˚. The diameter of the red circles approximately represents a 12˚error band around the AGN.

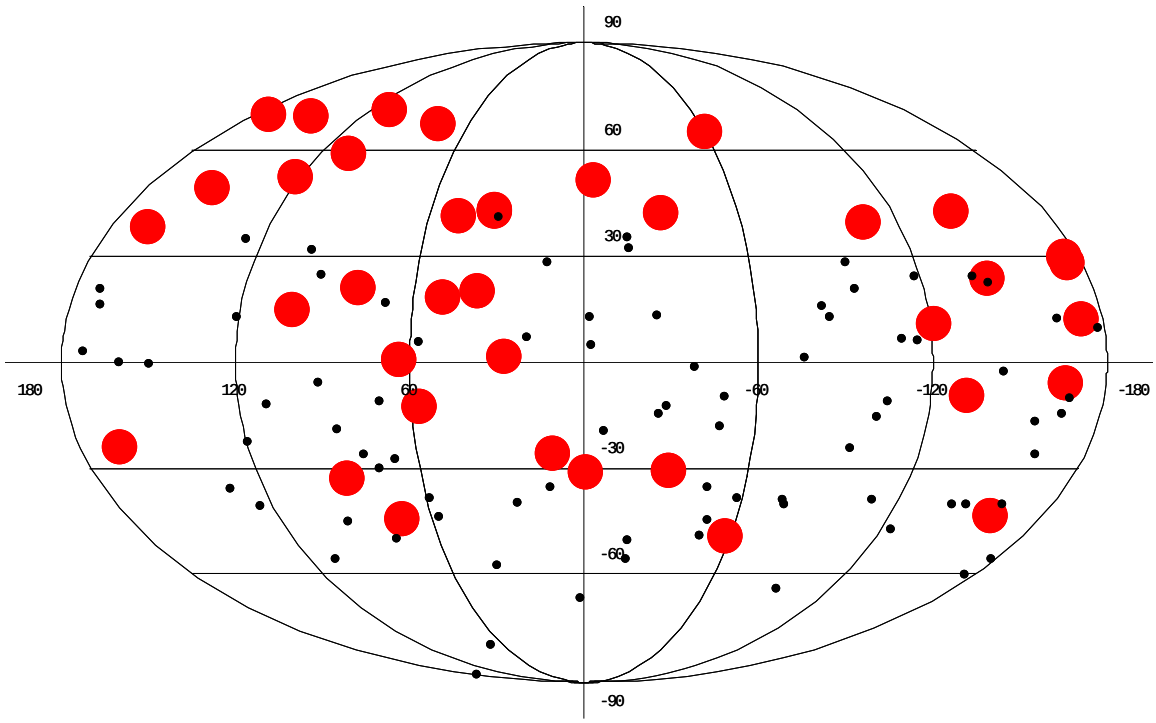

Figure 27. Sky map of AGN (red dots) and neutrino sources having energy ≥ 100 GeV and angular error ≤ 6˚. The diameter of the red circles approximately represents a 12˚error band around the AGN.

## VIII. Conclusion

There is theoretical support for Active Galactic Nuclei as the source of high energy neutrinos. If the theory is correct, AGN should appear to be point sources for muons produced by high energy neutrinos. However, neither the MINOS detector data used in this study nor results from similar studies at other worldwide neutrino detector sites have provided convincing evidence for the theory. Specifically, this study did not produce results that exhibited clustering of high energy neutrino point sources around known AGN. Expanded projects under construction at IceCube and ANTARES include plans to continue searching by using larger volume detectors. Perhaps there are many more AGN than we have currently catalogued that serve as sources for the high energy neutrinos that we seem to project using present day detectors.

## IX. Bibliography


[1] Braun et al., Methods for point source analysis in high energy neutrino telescopes, *Astroparticle Physics* 29 (2008) 299-305.
[2] Gelmini, Kusenko, Weiler, Through Neutrino Eyes, *Scientific American* 302, 5 (May 2010) 38-45.
[3] Abraham et al., Correlation of the highest-energy Cosmic Rays with Nearby Extragalactic Objects, Science 318 (9 November 2007) 938-943.
[4] DeMuth, A Search for Neutrinos from Active Galactic Nuclei, PhD Thesis, University of Minnesota, (August 1999).
[5] Ambrosio et al., Measurement of the energy spectrum of underground muons at Gran Sasso with a transition radiation detector, The MACRO Collaboration, arXiv:hep-ex/9807009v1 (9 July 1998) 1-21.
[6] Abe et al., High Energy Neutrino Astronomy Using Upward-Going Muons in Super-Kamiokande-I, the Super-Kamiokande Collaboration, arXiv:astro-ph/0606413v2 (26 July 2006) 1-7.
[7] Thrane et al., Search for Astrophysical Neutrino Point Sources at Super-Kamiokande, The Astrophysical Journal, 704(10 October 2009) 503-512.
[8] Padovani, A statistical analysis of complete samples of BL Lacertae objects, Astronomy and Astrophysics 256 (1992) 399-407
[9] Michael et al., The magnetized steel and scintillator calorimeters of the MINOS experiment, Nuclear Instuments & Methods in Physics Research, Elsevier, arXiv:0805.3170v2 (1 August 2008) 190-228.
[10] The Sudbury Neutrino Observatory, Sudbury, Ontario, Canada, http://www.sno.phy.queensu.ca/
[11] Reprint from National Science Foundation, http://www.nsf.gov/pubs/1996/nstc96rp/sb5.htm
[12] Urry and Padovani, Unified Schemes for Radio-Loud Active Galactic Nuclei, Publications of the Astronomical Society of the Pacific,v107,715(September 1995) 805.
[13] Abraham et al., Correlation of the highest-energy Cosmic Rays with Nearby Extragalactic Objects, Science 318 (9 November 2007) 939.
[14] Waste Isolation Pilot Plant, U.S. Department of Energy, http://www.wipp.energy.gov/science/dbdecay/dbdecay.htm
[15] Abraham et al., Correlation of the highest-energy Cosmic Rays with Nearby Extragalactic Objects, Science 318 (9 November 2007) 941.
[16] Andres et al., Results from the AMANDA High Energy Neutrino Detector, arXiv:astro-ph/0009242v1, (15 September 2000) 1-2.
[17] Podovani and Giommi, A sample-oriented catalogue of BL Lacertae objects, Royal Astronomical Society 277, (1995) 1477.
[18] Kuehn, The Search for Neutrinos from Gamma-Ray Bursts with AMANDA, 29th International Cosmic Ray conference Pune (2005) 5, 131-134.

[19] Lambard, Status of the ANTARES Neutrino Telescope and Prospects for Dark Matter Searches, Centre de Physique des Particules de Marseille, Marseille, France (January 2008)
[20] Smoot, Neutrino Astrophysics, http://aether.lbl.gov/www/projects/neutrino/
[21] DeMuth, A Search for Neutrinos from Active Galactic Nuclei, PhD Thesis, University of Minnesota, (August 1999), 102.
[22] DeMuth, A Search for Neutrinos from Active Galactic Nuclei, PhD Thesis, University of Minnesota, (August 1999), 115.
[23] The SNO Homepage, http://www.sno.phy.queensu.ca/ (2010).
[24] Besson et al., Neutrinos, Proceedings of the National Academy of Sciences of the United States of America, vol. 96 no. 25 (December 1999), 14202.
[25] Ambrosio et al., Neutrino Astronomy with the MACRO Detector, The Astrophysical Journal, 546 (January 2001) 1042
[26] Ambrosio et al., Neutrino Astronomy with the MACRO Detector, The Astrophysical Journal, 546 (January 2001) 1052
[27] DeMuth et al., Horizontal Muons and a search for AGN Neutrinos in Soudan 2, Elsevier, arXiv:hep-ex/0304016v2 (8 Jul 2003) 17.
[28] Summary of the MINOS Proposal, A Long -baseline Neutrino Oscillation Experiment at Fermilab, http://hepr5.physics.tamu.edu/minos.htm (March 1995)
[29] Achterberg et al., On the selection of AGN neutrino source candidates for a source stacking analysis with neutrino telescopes, arXiv:astro-ph/0609534 v1, (19 September 2006) 7.